


Modeling thermal inkjet and cell printing process using modified pseudopotential and thermal lattice Boltzmann methods

Salman Sohrabi^{1,*} and Yaling Liu^{2,†}

¹Lewis-Sigler Institute for Integrative Genomics, Princeton University, Princeton, New Jersey 08544, USA

²Department of Mechanical Engineering and Mechanics, Bioengineering Program, Lehigh University, Bethlehem, Pennsylvania 18015, USA

 (Received 22 August 2017; revised manuscript received 10 December 2017; published 12 March 2018)

Pseudopotential lattice Boltzmann methods (LBMs) can simulate a phase transition in high-density ratio multiphase flow systems. If coupled with thermal LBMs through equation of state, they can be used to study instantaneous phase transition phenomena with a high-temperature gradient where only one set of formulations in an LBM system can handle liquid, vapor, phase transition, and heat transport. However, at lower temperatures an unrealistic spurious current at the interface introduces instability and limits its application in real flow system. In this study, we proposed new modifications to the LBM system to minimize a spurious current which enables us to study nucleation dynamic at room temperature. To demonstrate the capabilities of this approach, the thermal ejection process is modeled as one example of a complex flow system. In an inkjet printer, a thermal pulse instantly heats up the liquid in a microfluidic chamber and nucleates bubble vapor providing the pressure pulse necessary to eject droplets at high speed. Our modified method can present a more realistic model of the explosive vaporization process since it can also capture a high-temperature/density gradient at nucleation region. Thermal inkjet technology has been successfully applied for printing cells, but cells are susceptible to mechanical damage or death as they squeeze out of the nozzle head. To study cell deformation, a spring network model, representing cells, is connected to the LBM through the immersed boundary method. Looking into strain and stress distribution of a cell membrane at its most deformed state, it is found that a high stretching rate effectively increases the rupture tension. In other words, membrane deformation energy is released through creation of multiple smaller nanopores rather than big pores. Overall, concurrently simulating multiphase flow, phase transition, heat transfer, and cell deformation in one unified LB platform, we are able to provide a better insight into the bubble dynamic and cell mechanical damage during the printing process.

DOI: [10.1103/PhysRevE.97.033105](https://doi.org/10.1103/PhysRevE.97.033105)

I. INTRODUCTION

Differently from conventional computational fluid dynamics methods [1–4], the lattice Boltzmann method (LBM) is based on mesoscopic kinetic equations in which the collective behavior of the particle distribution function (PDF) is used to simulate the continuum mechanics of the system [5,6]. An LBM has many advantages, such as easy implementation of various physical phenomena and fully parallel algorithms [7]. Among various LB methods, the pseudopotential model is simpler and more efficient in simulating a high-density ratio multiphase flow system [5]. It also has a lower computation cost compared to interface-capturing methods such as volume-of-fluid (VoF) and level set methods [8]. The Shan and Chen (S-C) model [9] and the free energy model by Swift *et al.* [10] are two major pseudopotential LBMs. A single-component pseudopotential LBM is capable of simulating phase transition through incorporation of the nonideal equation of state (EOS), such as those of Carnahan-Starling, Peng-Robinson (P-R), van der Waals, and Redlich-Kwong [8]. Among them, P-R EOSs are proven to have the best thermodynamic consistency [5].

The stability issue is the main setback limiting the application of the pseudopotential model to most real multiphase flow systems with a high density ratio and phase transition.

The major source of instability is a nonzero vortex-like fluid velocity in the vicinity of the phase interface which indicates the deviation from the real physical situation [11]. The so-called spurious currents drastically increase at lower temperatures (high-density ratios). Therefore, achieving a stable solution at room temperature is challenging. The main criteria to assess pseudopotential LBMs are maximum achievable density ratio or lowest realizable temperature. Various EOSs and formulations for interparticle interaction forces have been tested to increase stability [8].

Using P-R EOSs, the exact difference method, and a scheme for derivation of interparticle interaction force, Gong and Cheng [8] reported a lowest achievable temperature of $0.58T_c$. Later Kupershtokh *et al.* [12] overcame this limitation and were able to achieve liquid-to-vapor density ratios as big as 10^7 . Hu *et al.* [7] furthered this approach to demonstrate the feasibility of reaching temperatures as low as $0.2T_c$ with a density ratio of 10^9 . However, their major setback in this approach is compromising surface tension and an increase in interface thickness. In these studies, models are evaluated by comparing the coexistence curves obtained from the simulation with the theoretical one predicted by the Maxwell equal-area construction. To the best of our knowledge, these pseudopotential models have not yet been applied to the real multiphase flow systems at ambient temperature.

In this study, we used a reliable and stable modified formulation to minimize a spurious current at different saturation tem-

*sohrabi@princeton.edu

†yal310@lehigh.edu

peratures. Thermal LBM is also coupled with a pseudopotential model evolving at the same pace as the particle distribution function. The spatial and temporal changes of temperature are implemented through EOSs while flow information is used to update the temperature distribution. To demonstrate the capabilities of proposed model, our modified formulations are used to simulate the thermal injection process.

Inkjet printers are capable of delivering microdroplets at low manufacturing cost in applications such as additive manufacturing, bioprinting, and cell patterning [13,14]. Due to the low cost and high quality, thermal-type inkjet printers are popular [15]. In thermal bubble injection, a 3–6 μs width pulse wave with a frequency of 1–5 kHz is applied to instantly heat the liquid in a reservoir and nucleate bubble vapor, providing the pressure pulse necessary to eject a drop of ink out of the nozzle [16]. The size of droplets varies according to the applied temperature gradient, frequency of current pulse, and ink viscosity. To visualize the explosive vaporization process, complex formulations are needed to capture the phase separation/transition as well as heat transfer at the liquid-vapor interface [16]. Because of the high pressure in a superheated vapor bubble, the compressibility effect also should be included during instantaneous nucleation [17]. Due to this level of complexity, realistic simulation of the thermal injection process can be challenging.

Both level-set and VoF methods have been applied in simulations of droplet ejection [16–19]. These methods treat vapor region as a cavity and adopt the Clausius-Clapeyron equation to predict bubble pressure [16]. However, in coupled pseudopotential-thermal LBM, only a heat pulse is needed to be applied on a boundary, and everything else, e.g., bubble nucleation, growth, and collapse, are being taken care of by one set of formulations. The simplicity of our approach distinguishes it from other conventional interface-capturing methods [20–23].

Inkjet printing has been successfully applied for printing sophisticated patterns of biomolecules on various substrates [14,24,25]. However, there are concerns that the printing process may cause cell damage or death. In bioprinters, bio-ink in the cartridge is forced through a microfluidic chamber to an output orifice. Among different printing methods, cell membranes are more likely to be damaged in piezoelectric inkjet printers due to the range of frequencies used [24,26]. Although the temperature is locally increased to 300°C for a few microseconds in thermal inkjet printers, the overall temperature only rises 4–10°C and an average cell viability of

90% can be achieved [26]. In this study, we specifically look at cell deformation and membrane mechanical damage as the ink squeezes out of the thermal inkjet print head. To incorporate the cell body, a spring network (SN) model is coupled with pseudopotential LBM through an immersed boundary method [27–29]. By coupling these models, the injection dynamic and cell deformation at high speed can be visualized. In the following, first the proposed model is described and validated. Then, after discussing the results of injection simulation, cell deformation and damage are examined.

II. METHOD

In this study, pseudopotential LBM is used to model the phase transition in high-density ratio flow systems [5]. Moreover, thermal LBM is utilized to solve energy equation. To incorporate the cell in particulate flow [27,28], the SN model is also coupled with pseudopotential LBM. In what follows, these methods and relevant formulations are discussed.

A. Pseudopotential LBM

In standard lattice Boltzmann theory, the Bhatnagar-Gross-Krook (BGK) scheme describes the evolution of PDF, $f_i(x, t)$, at phase space (x, \vec{c}_i) at time t , where \vec{c}_i is the discretized velocity. The LBM dynamics involve streaming and collision steps:

$$\begin{aligned} f_i(x + \Delta t \vec{c}_i, t + \Delta t) \\ = f_i(x, t) - \frac{1}{\tau_f} [f_i(x, t) - f_i^{\text{eq}}(x, t)] + \Delta f_i(x, t), \quad (1) \\ f_i^{\text{eq}} = \omega_i \rho \left[1 + \frac{e_i \cdot u}{c_s^2} + \frac{(e_i \cdot u)^2}{2c_s^4} - \frac{u^2}{2c_s^2} \right], \quad (2) \end{aligned}$$

where $f_i^{\text{eq}}(x, t)$ is its corresponding equilibrium PDF, τ_f is the PDF relaxation time, c_s is the speed of sound in the LB scheme, and i is the number of discrete particle velocities. Macroscale density and velocity can be obtained as

$$\rho(x, t) = \sum_i f_i(x, t), \quad (3)$$

$$\rho(x, t) \vec{u}(x, t) = \sum_i f_i(x, t) \vec{c}_i. \quad (4)$$

The weighting factor and discrete velocity for D3Q19 lattice models are given as

$$e_i = \begin{cases} (0, 0, 0) & \alpha = 0, \\ (\pm 1, 0, 0)c, (0, \pm 1, 0)c, (0, 0, \pm 1)c, & \alpha = 1, 2, \dots, 6, \\ (\pm 1, \pm 1, 0)c, (\pm 1, 0, \pm 1)c, (0, \pm 1, \pm 1)c, & \alpha = 7, 8, \dots, 18, \end{cases} \quad (5)$$

$$\omega_i = \begin{cases} 1/3 & \alpha = 0, \\ 1/18 & \alpha = 1, 2, \dots, 6, \\ 1/36 & \alpha = 7, 8, \dots, 18. \end{cases} \quad (6)$$

The total force acting on a fluid particle in a multiphase flow may originate from different sources:

$$F_T = F_{\text{int}} + F_s + F_g + F_{\text{cell}}, \quad (7)$$

where F_s is the solid-fluid interaction force, F_{int} is the interparticle interaction forces, F_{cell} is the cell-fluid interaction force, and F_g represents gravitational force. In this study, the exact difference method (EDM) is used to incorporate the force term into Eq. (1) through Δu . $\Delta f_i(x, t)$ in EDM can be calculated as

$$\Delta f_i(x, t) = f_i^{\text{eq}}(\rho(x, t), u + \Delta u) - f_i^{\text{eq}}(\rho(x, t), u), \quad (8)$$

where $\Delta u = F_T \cdot \Delta t / \rho$ is the velocity change due to the body force during the lattice time step (δ_t). EDM was proposed by Kupershtokh and Medvedev [12] where the body force term is added directly to the right-hand side of Eq. (1) and there is no need to discretize the body force. There are also other methods to incorporate the force term such as the velocity-shifting method and discrete force method [8]. More detailed information concerning these approaches can be found in Ref. [8], where it is shown that EDM has better accuracy and stability. In the following, all forces acting on particulate flow are discussed in detail.

B. Interparticle interaction forces

Microscopically, the segregation of a fluid system into different phases is due to the interparticle forces; see Eq. (7). In the pseudopotential model, the interparticle interaction force, F_{int} , is responsible for phase separation. In this study, modified the S-C interparticle interaction force scheme is used:

$$F_{\text{int}}(x) = -\beta c_0 g \psi(x) \nabla \psi(x) - (1 - \beta) c_0 g \nabla \psi(x)^2 / 2, \quad (9)$$

where β is the weighting factor, c_0 is 6.0 for D3Q19 lattice structure, and $\psi(x)$ is effective mass which reflects the intensity of the interparticle interaction. The value of $\beta = 1.16$ is optimized to best match the Maxwell construction [30]. Equation (9) can be discretized as

$$F_{\text{int}}(x) = -\beta \psi(x) \sum_{x'} G(x, x') \psi(x') (x' - x) - \frac{1 - \beta}{2} \sum_{x'} G(x, x') \psi^2(x') (x' - x), \quad (10)$$

where $G(x, x')$ and $\psi(x)$ are given by

$$G(x, x') = \begin{cases} g_1, & |x' - x| = 1 \\ g_2, & |x' - x| = \sqrt{2} \\ 0, & \text{otherwise,} \end{cases} \quad (11)$$

$$\psi(\rho) = \sqrt{\frac{2(p - \rho c_s^2)}{c_0 g}} \quad (12)$$

with $g_1 = g$, $g_2 = g/2$ for the D3Q19 scheme. In the multicomponent S-C model, Eq. (12) is simplified as $\psi(\rho) = \rho_0 [1 - \exp(-\rho/\rho_0)]$, which gives a nonmonotonic pressure-density relationship. In this case, the temperature is constant and equal to $T = -1/g$ in a lattice unit. Also, the role of pressure is dictated through g while $\rho_c = \rho_0 \ln 2$ and $g_c = -2/(9g_0)$. Hence, for $g < g_c$ two densities of the same material can coexist at a single pressure and temperature. However, by changing the form of $\psi(\rho)$, a different EOS can be theoretically obtained. In this study, the P-R EOS, which is more accurate

and popular for water, is used:

$$p = \frac{\rho RT}{1 - b\rho} - \frac{a\rho^2 \varepsilon(T)}{1 + 2b\rho - b^2\rho^2}, \quad (13)$$

where $\varepsilon(T) = [1 + (0.37464 + 1.54226\omega - 0.26992\omega^2)]^2$, with $\omega = 0.344$ being the acentric factor for water. By setting the first and second derivatives of the pressure to zero, $a = 0.4572R^2T_c^2/P_c$ and $b = 0.0778RT_c/P_c$ can be derived. Since the lattice sound speed is $c_s = \sqrt{3RT_c} = 1/\sqrt{3}$, by choosing $R = 1$, $a = 2/49$, and $b = 2/21$, critical temperature, pressure, and density in the lattice unit can be accordingly calculated as $T_c = 0.0729$, $P_c = 0.0596$, and $\rho_c = 2.3382$.

C. Solid-fluid interaction force

The interaction force [Eq. (7)] between the solid and fluid is given by

$$F_s(x) = -(1 - e^{-\rho(x)}) \sum_i g_s \omega_i s(x + e_i \delta_t) \cdot e_i \delta_t, \quad (14)$$

where g_s is the fluid-solid interaction and can be adjusted for proper contact angle. The indicator function, $s(x)$, is equal to 1 and 0 when x is in solid and fluid, respectively. Furthermore, the gravity force [Eq. (7)] is given by

$$F_g(x) = G \cdot [\rho(x) - \rho_{\text{ave}}], \quad (15)$$

where G is the acceleration of gravity and ρ_{ave} is the average density at each time step.

D. Thermal lattice Boltzmann method

The temperature in an EOS can be derived by solving an energy equation [31]

$$\frac{\partial T}{\partial t} + \nabla \cdot (UT) = \nabla \cdot (\alpha \nabla T) + \phi, \quad (16)$$

where $\alpha = \frac{\lambda}{\rho c_v}$ is the thermal diffusivity. To solve Eq. (16) with thermal LBM, a second set of distribution function is introduced:

$$T(x, t) = \sum_i g_i(x, t). \quad (17)$$

Similarly, the temperature distribution function evolves by

$$g_i(x + \Delta t \vec{c}_i, t + \Delta t) - g_i(x, t) = -\frac{1}{\tau_T} [g_i(x, t) - g_i^{\text{eq}}(x, t)] + \Delta t \omega_i \phi, \quad (18)$$

where τ_T is thermal the relaxation time, ϕ is the source term responsible for phase change, and $g_i^{\text{eq}}(x, t)$ is the equilibrium temperature distribution function given by

$$g_i^{\text{eq}} = \omega_i \rho \left[1 + \frac{e_i \cdot u}{c_s^2} \right]. \quad (19)$$

The source term in Eq. (16) represent heat storage and release during the phase transition process. To derive Φ in terms of p , T , and ρ , an entropy balance equation, $\rho T \frac{ds}{dt} = \nabla \cdot (\lambda \nabla T)$, is used in conjunction with thermodynamic relations [32]. Gong and Cheng [32] demonstrated that the entropy balance equation can be rewritten in the form of a heat transport

equation where the last two terms represent the source term responsible for phase change. Finally, they derived a simplified equation for Φ , which was written as

$$\phi = T \left[1 - \frac{1}{\rho c_v} \left(\frac{\partial p}{\partial T} \right)_v \right] \nabla \cdot U, \quad (20)$$

where c_v is specific heat capacity.

E. Model parameters

The kinematic viscosity and thermal diffusivity in lattice unit are given by

$$\nu_{LB} = c_s^2 (\tau_P - \frac{1}{2}) \Delta t_{LB}, \quad (21)$$

$$\alpha_{LB} = c_s^2 (\tau_T - \frac{1}{2}) \Delta t_{LB}, \quad (22)$$

where τ_P and τ_T are relaxation parameters in pseudopotential and thermal LBM, respectively. Reynolds and Prandtl dimensionless numbers bring physical parameters to lattice units and can be defined as

$$\text{Re} = \frac{U_{\text{phy}} L_{\text{char}}}{\nu_{\text{phy}}} = \frac{U_{LB} L_{LB}}{\nu_{LB}}, \quad (23)$$

$$\text{Pr} = \frac{\nu_{\text{phy}}}{\alpha_{\text{phy}}} = \frac{2\tau - 1}{2\tau_T - 1}. \quad (24)$$

To convert physical parameters to lattice units, characteristic time, length, mass, and temperature should be calculated first. Characteristic length and time scales are given as

$$U_{\text{phy}} = \frac{L_{\text{phy}}}{t_{\text{phy}}} = \frac{N_{\text{mesh}} \times \Delta x_{\text{char}}}{N_{\text{iter}} \times \Delta t_{\text{char}}},$$

$$U_{LB} = \frac{L_{LB}}{t_{LB}} = \frac{N_{\text{mesh}} \times \Delta x_{LB}}{N_{\text{iter}} \times \Delta t_{LB}}, \quad (25)$$

where N_{mesh} is the number of mesh in a characteristic length scale, and N_{iter} is the number of iteration during a characteristic time scale. Generally, we assume $\Delta t_{LB} = 1$, $\Delta x_{LB} = 1$, and $c_s = 1/\sqrt{3}$. Using the discussed relations, the physical time step can be derived as

$$\Delta t_{\text{phy}} = \frac{L_{\text{phy}}^2}{N_{\text{mesh}}^2} \times \frac{(\tau_P - 0.5)/3}{\nu_{\text{Ref}}} \quad \text{or}$$

$$\Delta t_{\text{phy}} = \frac{L_{\text{phy}}^2}{N_{\text{mesh}}^2} \times \frac{(\tau_T - 0.5)/3}{\alpha_{\text{Ref}}}. \quad (26)$$

It can be seen that by setting L_{phy} , N_{mesh} , and kinematic viscosity (or thermal diffusivity), the time step in a physical system can be simply calculated. The acceptable range for both relaxation times is between 0.5 and 2. The closer it gets to 0.5, the more unstable LB simulation will be. Additionally, pseudopotential and thermal LBM are needed to evolve in the same pace. We also know that the value of kinematic viscosity and thermal diffusivity may vary orders of magnitude depending on density (vapor and liquid) and temperature at different regions of the computational domain. To address these issues, the maximum kinematic viscosity (or thermal diffusivity) within a desired temperature range should be identified first and set as $\tau = 1.99$. Based on this assumption,

characteristic time and length in both physical and lattice units can be accordingly calculated. Furthermore, critical density and temperature in the lattice unit are set to 0.0729 and 2.3382 in pseudopotential LBM. Thus, by using $\rho_c = 322 \frac{\text{kg}}{\text{m}^3}$ and $T_c = 647.096\text{K}$ in a physical system, characteristic mass and temperature can also be calculated and then used to convert all other physical parameters. Physical parameters at the liquid-vapor interface are estimated as

$$\chi = \chi_{\text{liquid}} \frac{\rho - \rho_{\text{vapor}}}{\rho_{\text{liquid}} - \rho_{\text{vapor}}} + \chi_{\text{vapor}} \frac{\rho_{\text{liquid}} - \rho}{\rho_{\text{liquid}} - \rho_{\text{vapor}}}. \quad (27)$$

Viscosity and thermal diffusion are temperature- and density-dependent physical properties. Thus, their values in physical units constantly change during a phase transition or temperature fluctuation. Thus, it is imperative to adjust their value in a lattice unit accordingly. We will use these fixed characteristic scales. For instance, the temperature rise in a computational domain will result in a decrease of thermal diffusion. Thus, the value of τ_T should be subsequently updated because of this change.

F. Spring network model

Mechanical properties of cells depend on the mechanical properties of the subcellular components such as cytoplasm, nucleus, cell membrane, and cytoskeleton, as well as their distribution, linkage, and structure within the cell. Due to heterogeneous intracellular structures, proper modeling of cell mechanics is very challenging. Particular structures such as the spring connected network model (SN) have been widely used for simulating blood cells [33–35]. In the case of regular cells, the membrane and nuclear envelope can be modeled as a SN while actin fibers are represented by a linear spring [36]. In a SN the membrane is composed of a set of vertex nodes $X_i, i \in \{1 \dots N_V\}$ that are connected by springs [36,37] forming a two-dimensional triangulated network. Elastic resistances to changes in bending, stretching, and surface area can be implemented through potential energies:

$$V(\{x_i\}) = V_{\text{in-plane}} + V_{\text{bending}} + V_{\text{area}} + V_{\text{volume}}. \quad (28)$$

The in-plane energy term characterizes the elastic energy stored in the membrane. The bending potential corresponds to bending stiffness of membrane, while the last two potential terms conserve volume and surface area of lipid bilayer. More detailed information about these energy terms can be found in Refs. [33,36,38]. The nodal forces corresponding to each energy can be calculated as $f_i = -\partial V\{x_i\}/\partial x_i$. To avoid complexity, the nuclear envelope and actin fibers are not considered in our current cell model.

Using the immersed boundary method (IBM), the parametric surface $X(s,t)$ exerts a force density on the fluid, $F_c(x,t)$, to represent the effect of a solid body [39,40]. Similarly, the solid velocity, $u(X,t)$, will be interpolated from the local fluid nodes and will be used to update solid nodes [27,41]:

$$F_c(x,t) = \int f(s,t) \delta[x - X(s,t)] ds, \quad (29)$$

$$u(X,t) = \int u(x,t) \delta[x - X(s,t)] dx,$$

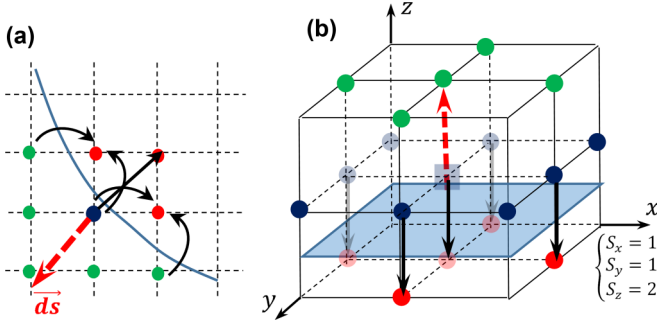


FIG. 1. Calculation of interparticle force on boundary nodes using ghost points (shown in red).

$$\delta(r) = \begin{cases} \frac{1}{4} \left[1 + \cos\left(\frac{\pi r}{2}\right) \right] - 2 & 2 \leq r \leq 2 \\ 0 & \text{otherwise.} \end{cases} \quad (30)$$

Our cell model is benchmarked with optical tweezer experimental data in our previous work [33,41] where we studied red blood cell (RBC) damage. In the same study, the deformation of RBCs under pure shear flow is also investigated where the results for the oscillation period agreed with experiments of Abkarian *et al.* [42].

G. Boundary conditions

In this study, Zou-He bounce-back rules [43] are used to enforce nonslip wall boundary condition. Furthermore,

$$F_{\text{int}}^j(x) = S^j(x) \left[-\beta \psi(x) \sum_{x'} G(x, x') \psi(x') (x' - x) - \frac{1 - \beta}{2} \sum_{x'} G(x, x') \psi^2(x') (x' - x) \right], \quad (33)$$

where $S^j(x)$ represents a correction coefficient along the $j = x, y, z$ axis. $S^j(x)$ is one except for directions that have ghost lattice points in either direction [$S^j(x) = 2$]. It should be noted that the normal component of interparticle force at the wall should also be zero. This condition at curved boundaries can be simply enforced through updating $\vec{F}_{\text{int}} = \vec{F}_{\text{int}} - |\vec{F}_{\text{int}} \cdot \vec{d}s| \vec{d}s$ where $\vec{d}s$ is a unit normal vector.

III. MODEL VALIDATION

The $p - v$ curve at a subcritical temperature allows the coexistence of liquid and vapor densities at a single pressure and temperature. Gibbs free energy has equal values at liquid and vapor phases in equilibrium as shown in Fig. 2. This is the basic idea for the Maxwell construction of EOS, $\int_{v_l}^{v_g} P dv = P_s(v_g - v_l)$ where v_g and v_l are the specific volume of saturated liquid and vapor, respectively. Using a P-R EOS, system pressure versus densities can be plotted at different saturation temperatures as shown in Fig. 2. It can be seen that the density ratio increases as the temperature decreases; for instance, at $0.5T_c$, the density ratio is $\rho_l/\rho_v = 1.08 \times 10^4$.

The stability issue is the main reason limiting the application of the pseudopotential model to most real multiphase flow systems at room temperature. The source of the instability

constant surface temperature is applied using the Dirichlet boundary condition:

$$g_i^*(x, t + \Delta t) = [\omega_i + \omega(-\Delta t \vec{c}_i)] T_{\text{wall}} - g(x, -\Delta t \vec{c}_i, t), \quad (31)$$

where T_{wall} is the temperature at the wall. To apply a heat pulse, the Neumann boundary condition is utilized:

$$g_i^*(x, t + \Delta t) = [\omega_i + \omega(-\Delta t \vec{c}_i)] \left[\sum_i g_i(x, t) + \frac{Q_s}{k} \right] - g(x, -\Delta t \vec{c}_i, t), \quad (32)$$

where Q_s (W/m²) is the heat flux from a heater resistor and k (W/m k) is thermal conductivity. At each node on the heating element, the temperature is used to first evaluate k at both phases, then Eq. (27) is used to estimate actual thermal conductivity. Other model parameters such as kinematic viscosity, thermal diffusivity, and specific heat capacity also strongly depend on temperature and need to be continuously updated in the same manner.

To calculate interparticle force, the effective mass at all neighboring lattice nodes should be calculated first. But Eq. (10) can no longer be used for nodes on the wall. However, it can be modified in a way that eliminates the necessity for tedious computations. Calculated effective mass for nodes inside the domain can be simply copied to ghost lattice points on the other side of the wall as shown in Fig. 1. Thus, Eq. (10) can be modified as

is spurious currents which almost exponentially increase as temperature decreases [8]. Among various pseudopotential multiphase models, Gong and Cheng [8] modified Yuan and Schaefer's formulation [5] and showed that they could achieve

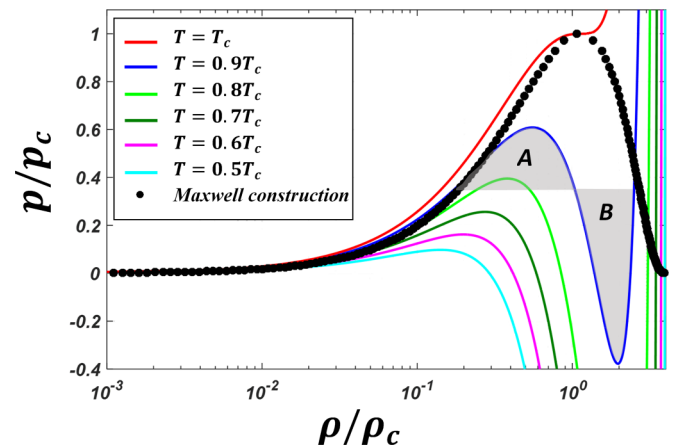


FIG. 2. Maxwell construction of the Peng-Robinson (P-R) EOS at various subcritical temperatures. Highest pressure at $T = T_c$ is shown with a red solid line (dark gray), while lowest pressure at $T = 0.5T_c$ is shown in a solid cyan line (light gray).

TABLE I. Model parameter in both lattice and reference units at different simulated temperatures.

T	τ^l	τ^v	τ_T^l	τ_T^v	ν_l^{Ref}	ν_v^{Ref}	α_l^{Ref}	α_v^{Ref}
$0.45T_c$	0.502	1.970	0.5003	1.979	1.0×10^{-6}	6.27×10^{-4}	1.08×10^{-7}	6.31×10^{-4}
$0.5T_c$	0.506	1.953	0.5014	1.526	5.5×10^{-7}	1.26×10^{-4}	1.22×10^{-7}	8.89×10^{-5}
$0.6T_c$	0.527	1.966	0.515	1.459	2.5×10^{-7}	1.32×10^{-5}	1.33×10^{-7}	8.63×10^{-6}
$0.7T_c$	0.528	1.973	0.522	1.109	1.7×10^{-7}	8.8×10^{-6}	1.36×10^{-7}	3.65×10^{-6}
$0.8T_c$	0.701	1.925	0.697	1.205	1.3×10^{-7}	9.5×10^{-7}	1.31×10^{-7}	4.7×10^{-7}

a minimum temperature of $0.58T_c$ using a P-R EOS and velocity shifting method. However, the spurious current is still high and the solution is very unstable. Additionally, the only way to achieve a stable solution at $0.58T_c$ is to gradually decrease the temperature. These limitations made the application of this model without proper modification very challenging.

To address this issue, Kupershtokh *et al.* [12] proposed reduced EOSs to achieve density ratios as high as 10^7 using vdW and mKM (Kaplun-Meshalkin) EOSs. Following similar principal, Hu *et al.* [7] investigated the effect of a reduced parameter on a spurious current and surface tension. In this approach, the pressure term can be modified as

$$\dot{p} = k' p = k' \left[\frac{\rho RT}{1 - b\rho} - \frac{a\rho^2 \varepsilon(T)}{1 + 2b\rho - b^2 \rho^2} \right], \quad (34)$$

where $k \leq 1$ represents the reduced parameter. The value of the reduced parameter does not influence the Maxwell construction of EOSs [7]. It should be noted that the introduced parameter effectively reduces spurious currents and enable us to simulate a liquid-vapor density ratio as high as 10^9 when $k' = 0.01$ [7]. The temperature was fixed in these studies as opposed to our case where we plan to use thermal LBM to calculate temperature.

The stability of the pseudopotential model can be evaluated by comparing the coexistence curves obtained from simulation with the theoretical one predicted by the Maxwell equal-area construction. To simulate the formation of a liquid droplet at a given temperature, the initial density distribution at the center is set slightly higher than the rest of the domain. Periodic boundary conditions are imposed on all directions where a $150 \times 150 \times 150$ lattice structure is chosen for

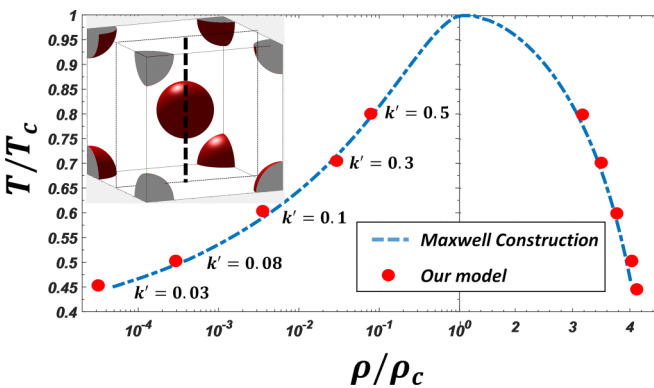


FIG. 3. Maxwell construction prediction for P-R EOS versus simulation results of our coupled pseudopotential-thermal model using reduced EOS. The relative density, ρ/ρ_c , is demonstrated in two linear and logarithmic scales at right and left, respectively.

computation. Particle and thermal relaxation times for both liquid and vapor phases are calculated as shown in Table I. By using proper values for a reduced parameter, the magnitude of spurious current can be controlled. Simulations were carried out for 40,000 time steps to ensure that the steady state was reached. At the steady state, liquid droplets (with density ρ_l) surrounded by the vapor (with density ρ_g) are formed in a computational domain as shown in Fig. 3. It is observed that our coupled pseudopotential-thermal model matches the Maxwell construction prediction for P-R EOS.

Mesh size is an important parameter influencing phase separation. To perform a mesh dependency study, simulations with different mesh densities were carried out at $T_{\text{init}} = 0.5T_c$ with $k' = 0.08$ as shown in Fig. 4. For mesh size bigger than 120, the vapor density solution matches the Maxwell construction prediction. Additionally, the interface thickness decreases as the mesh density increases. However, the spurious current is not influenced by mesh density. Theoretically, the reduced parameter will not influence phase separation dynamic [7], and it should only decrease spurious current. Figure 5 demonstrates the effect of a reduced parameter on liquid and vapor densities. At constant temperature $0.5T_c$, the thickness of the interface decreases to almost half by increasing k' from 0.05 to 0.1. However, a high spurious current in the $k' = 0.1$ case disturbs uniform temperature distribution. On the other hand, at a lower reduced parameter the interface thickness significantly increases, and one would need many more mesh node to acquire correct vapor density in saturated state.

The effect of temperature and reduced parameter on a maximum spurious current is also studied as shown in Fig. 6.

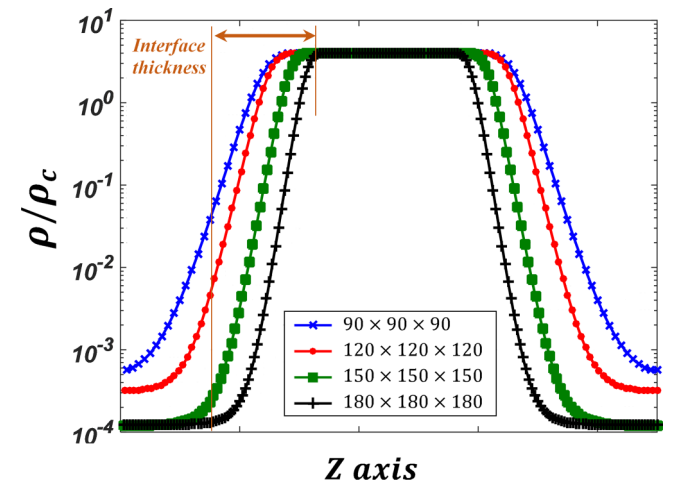


FIG. 4. Mesh dependency analysis of phase separation at $T_{\text{init}} = 0.5T_c$. Relative density data along dotted line shown in Fig. 3.

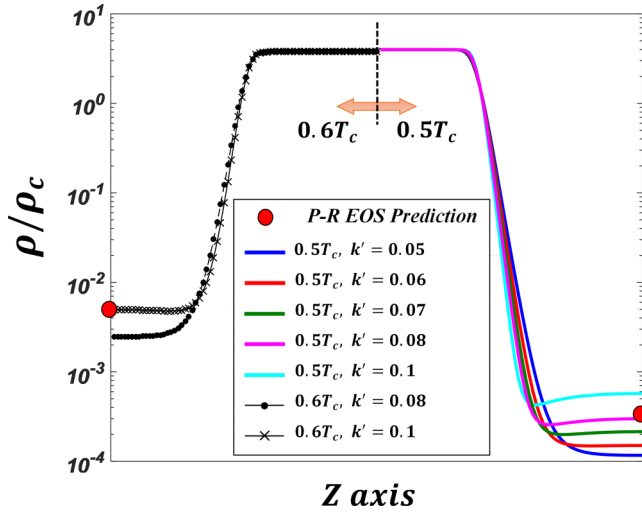


FIG. 5. Liquid-vapor separation for different reduced parameter. Mesh size is $150 \times 150 \times 150$. From highest density [at $T = 0.5T_c, k' = 0.1$, cyan (light gray)] to lowest density [at $T = 0.5T_c, k' = 0.05$, blue line (dark gray)].

It is observed that for $k' = 1$, our results match very well with the Gong and Cheng study for $0.6T_c, 0.7T_c$, and $0.8T_c$ [8]. As shown in Fig. 6, the spurious current at $0.6T_c$ ($U_s = 0.15$) is no longer negligible compared to the speed of sound, $c_s = 1/\sqrt{3}$. The high spurious current at the interface generates an unphysical temperature gradient. By keeping a spurious current under ~ 0.03 , cases with $k' = 0.08$ at $0.5T_c$ and $k' = 0.1$ at $0.6T_c$ are found to match the Maxwell construction prediction better as shown in Figs. 5 and 6. For spurious currents lower than ~ 0.03 , the magnitude of temperature fluctuation at the interface is also negligible, $\sim 0.002T_c$. On the other hand, a reduced parameter should be large enough to avoid a very thick phase interface. Thus, choosing the proper value for a reduced parameter when modeling a phase transition in a multiphase flow is critical.

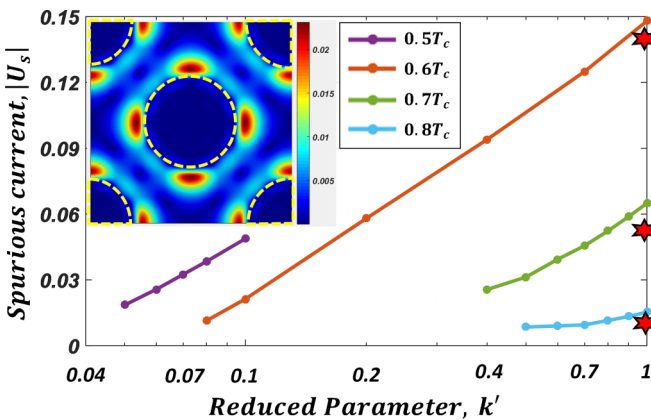


FIG. 6. Spurious current in lattice units for various temperatures and reduced parameters. The red stars represent the spurious current at $k' = 1$ using the original pseudopotential formulation by Gong and Cheng [8]. $0.5T_c$ and $0.8T_c$ are colored violet (dark gray) and blue (light blue), respectively. The velocity distribution contours demonstrate an unrealistic spurious current at the phase interface.

To benchmark the wall-fluid interaction, we have simulated droplet on a surface as shown in Figs. 7(a)–7(c). The liquid-solid interaction strength, g_s , represents the strength of the intermolecular force between wall and fluid. By tuning g_s , we can control the wettability of the surface or in other words the contact angle. The density distribution along the z axis is also demonstrated for cases with different contact angles as shown in Fig. 7(d). To demonstrate the capabilities of the discussed approach, the thermal ejection process is modeled as an example of a complex multiphase flow system.

IV. THERMAL INKJET PRINTER

To simulate the bioprinting process, the geometrical configuration of an HP60 inkjet cartridge is used where cells are ejected through a narrow nozzle channel with a diameter of $48\mu\text{m}$. The cross section of the HP60 nozzle plate and schematics of the computational model are presented in Figs. 8(a)–8(b). The computational domain consists of $120 \times 240 \times 600$ lattice nodes, and Zou-He bounce-back rules [43] are applied at all surfaces. In the HP60 inkjet cartridge, the heating resistors under each nozzle are stressed with a $3\mu\text{s}, \sim 10\frac{\text{V}}{250}\text{mA}$ pulse to boil the ink and eject the drop. This takes the resistor up above the superheating point of water and creates an almost explosive vapor bubble that ejects the ink droplet at $\sim 12\text{m/s}$. For water at atmospheric pressure, nucleate boiling occurs at $\sim 380\text{K}$. However, the liquid in a thermal inkjet printer begins to boil only when it is heated close to the superheated temperature of 580K . The reason is that the liquid is heated extremely quickly with a heat flux as high as $\sim 4.6 \times 10^8\text{W m}^{-2}$ [16]. Thus, the nucleation bubble instantaneously covers the surface of the heater in $\sim 0.01\text{ms}$ and the bubble pressure can reach as high as $\sim 8\text{--}12\text{MPa}$ [16]. The bubble then collapses, and the ink cavity refills with liquid. The initial pressure and volume of the vapor bubble depend on firing conditions such as voltage pulse and liquid temperature.

Because the superheated vapor bubble behaves like a compressible fluid during the grow and collapse cycle, it cannot be directly handled by incompressible flow solvers. To overcome this issue, the flow in the vapor domain is ignored in the literature and the vapor bubble is treated as a cavity so that the bubble can freely expand and shrink [44]. Thus, only the pressure information, force on the liquid surface, is passed onto the fluid solver. However, due to the high temperature and density gradient in the bubble region, the bubble dynamic might be different from what has been previously realized [13,16,44–46]. Due to the high dependency of local pressure, density, and temperature on each other, the EOS is needed to be directly implemented. Furthermore, the model should also be capable of simulating a phase transition. Thus, our modified pseudopotential LBM coupled with thermal LBM can nicely capture the nucleation flow dynamics during the injection process.

To simulate the thermal injection process at ambient temperature, a computational domain is needed to be initialized first where water and vapor phases are separated at the nozzle head. Initialization of thermal pseudopotential LBM is challenging since the simulation cannot be simply started by setting liquid and vapor densities at desired lattice nodes. The reason is that abrupt changes in density at the interface instantly diverge the

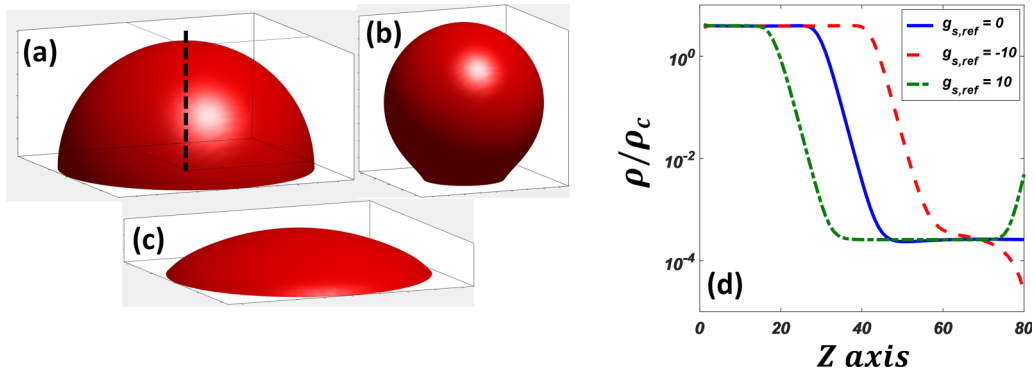


FIG. 7. Droplet on a surface for different liquid-solid interaction strengths: (a) $g_s = 0$, (b) $g_s = -10$, (c) $g_s = 10$. These simulations are carried out with an initial temperature of $0.5T_c$ with $120 \times 240 \times 600$ lattice nodes. (d) Relative density across the dashed line for various liquid-solid interaction strengths.

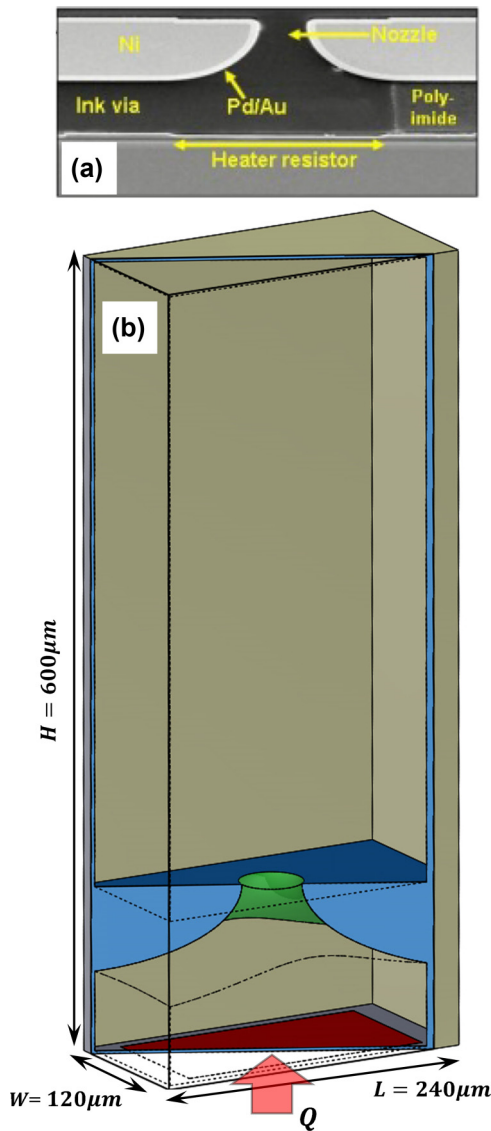


FIG. 8. (a) Cross section of the HP60 nozzle plate. (b) Schematics of the microinkjet nozzle in a computational model. Heating resistor is shown in red.

solution. One approach is starting the simulation at a higher temperature, e.g., $0.8T_c$, where the solution is significantly more stable, and then gradually decrease it. In this case, we may not be able to fully fill the reservoir with liquid or the droplet may be created outside of the reservoir. To address this issue, we first set the vapor density on all lattice nodes. Then the density of nodes inside the reservoir are gradually raised to the target liquid density as shown in Fig. 9.

As discussed before, the reduced parameter is introduced to maintain the spurious current within an acceptable range and avoid solution divergence. It is observed from Fig. 6 that different values of the reduced parameter can be used at different saturation temperatures. Therefore, the reduced parameter is assumed to linearly increase to one as the temperature reaches T_c as shown in Fig. 10. By doing this, we managed to avoid a high spurious current at the nucleation region. Although the formulations used to incorporate the phase transition, heat transfer, cell deformation, and solid-liquid-gas interaction in a

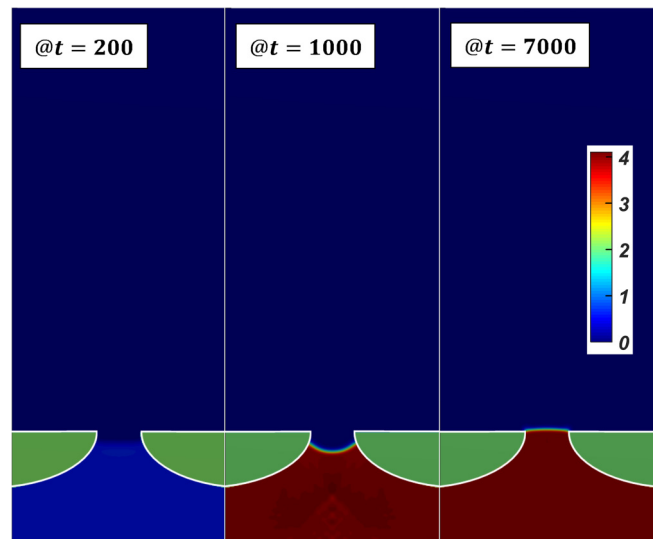


FIG. 9. Relative density distribution during initialization. $t_{\text{lattice}} = 7000$ marks $t = 0\text{s}$ in reference units.

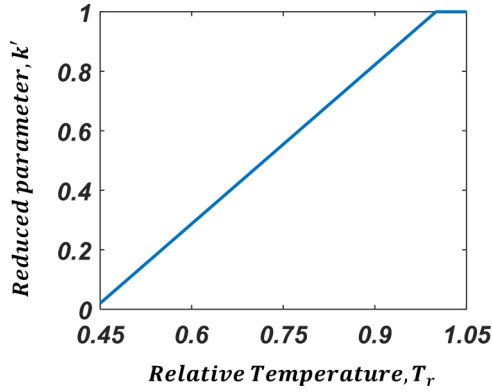


FIG. 10. Linear variation of reduced parameter versus relative temperature. k' equals 0.03 at $0.45T_c$.

curved geometry seem very complicated, the implementation in a LB platform is relatively simple; see Fig. 11. After calculating the interparticle interaction and wall, cell, and gravity forces, PDFs undergo collision and stream steps. Then, by inputting the heat flux at the boundary and calculating phase transition term, the thermal LBM is solved.

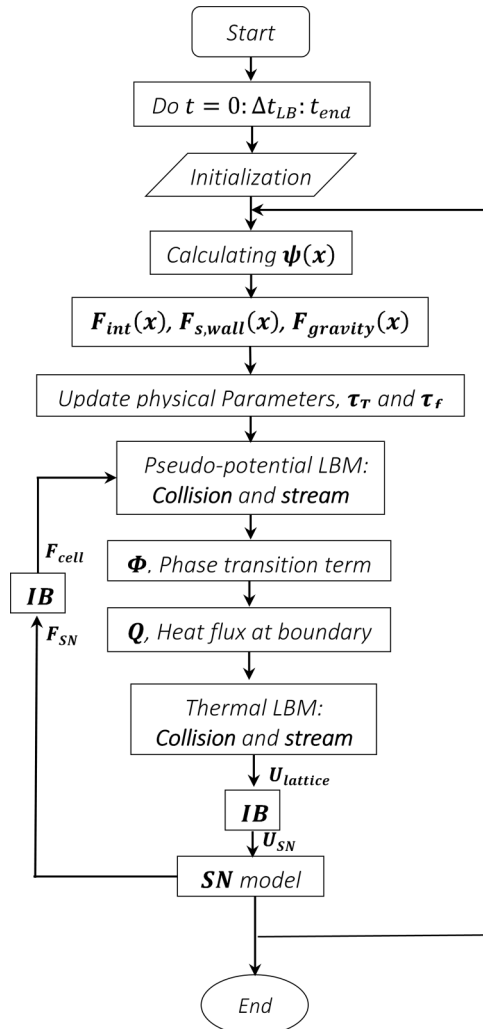


FIG. 11. Solution process flow chart.

TABLE II. Water thermal conductivity and specific heat at different temperatures.

T	k_l ($\text{W m}^{-1}\text{K}^{-1}$)	k_v ($\text{W m}^{-1}\text{K}^{-1}$)	$C_{p,l}$ ($\text{kJ kg}^{-1}\text{K}^{-1}$)	$C_{p,v}$ ($\text{kJ kg}^{-1}\text{K}^{-1}$)
$0.5T_c$	0.64	0.02	4.17	1.94
$0.6T_c$	0.68	0.026	4.23	2.14
$0.7T_c$	0.67	0.049	4.40	2.41
$0.8T_c$	0.627	0.06	4.80	3.84

After initialization, a thermal pulse of $\sim 8 \times 10^6 \text{ W m}^{-2}$ for $4 \mu\text{s}$ is applied to the heater element. It should be mentioned that during the injection process, temperature-dependent physical properties such as thermal diffusivity and viscosity (see Table I) are constantly being updated through relaxation parameters. Moreover, the relevant values for water thermal conductivity and specific heat at different temperatures are also listed in Table II. The simulation time step in physical units is 3.5 ns.

The time sequence of nucleation, bubble growth, droplet ejection, and bubble collapse processes is demonstrated in Fig. 12. Furthermore, the temperature distribution at different times is shown in Fig. 13. Videos of this process are also made available as Supplemental Material, which can provide a better understanding of the rapid explosive droplet injection process [47]. Supplemental video 1 demonstrates the density distribution during the droplet ejection process, and supplemental video 2 displays temperature distribution changes at any instance of time. At the beginning stage of the thermal pulse, the temperature of water in contact with the heater element is increasing relatively slow. However, right before the heat flux stops, the temperature of lattice nodes on the lower boundary drastically increase as shown in Fig. 13. For instance, the temperature of nodes on the heater element just before the end of the heat pulse is $\sim 1.5T_c$. However, bubbles start to form only $2 \mu\text{s}$ after the heat pulse stops as shown in Fig. 12. In a normal boiling situation, the small vapor and gas bubble trapped in cracks acts as a preexisting nucleus. In inkjet printing, bubbles are generated at superheated temperatures. Thus, the temperature distribution on the heater is the most important factor directly influencing bubble nucleation. Since the length of the heater pad is twice as big as its width, there are two places with a maximum local temperature at initial stages of simulation; see Fig. 13. These two local maxima are the main reason that we derive the formation of two bubbles instead of one. These two nucleated bubbles gradually grow and eventually aggregate to form one big bubble as it pushes the water droplet out of the nozzle. It should be noted that vapor is in its saturated state and will ultimately collapse as heat dissipates to the surrounding liquid. During the $4 \mu\text{s}$ collapse cycle, the bubble quickly disappears when it reaches its maximum volume at $t = 31 \mu\text{s}$ as shown in Fig. 14.

As discussed before, the reduced parameter is assumed to linearly increase with temperature. Bigger values for the reduced parameter drastically increases a spurious current and ultimately results in solution divergence. On the other hand, we could potentially use smaller reduced parameters. However, we needed to use a significantly finer mesh.

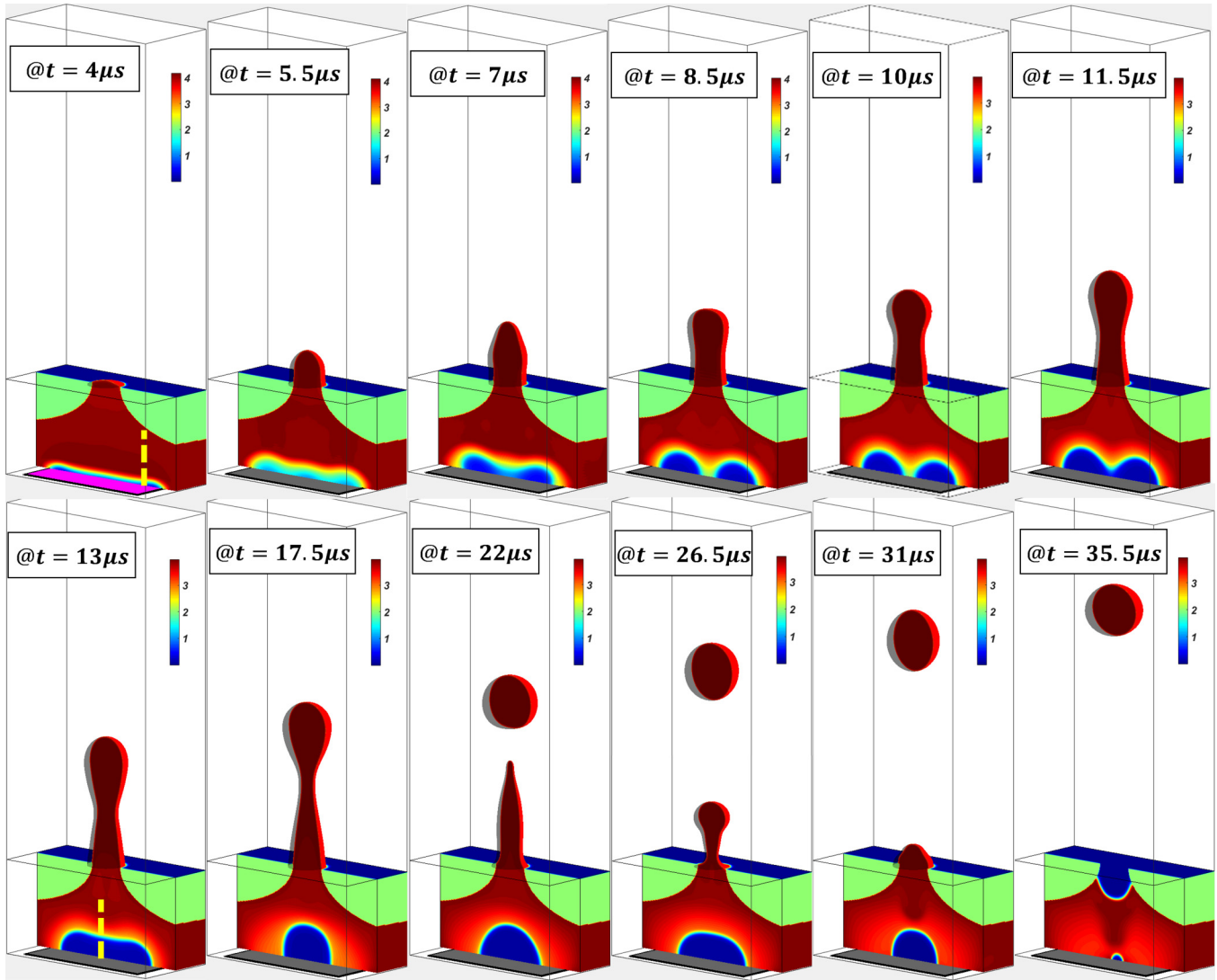


FIG. 12. Time sequence of droplet injection process at nozzle cross section. Color bar represents relative density.

The final speed of the projectile is approximately $\sim 12 \frac{\text{m}}{\text{s}}$, which agrees with previous numerical and experimental studies [13,17,44,45]. The drophead velocity at any instance of time is depicted in Fig. 15 where it is compared with experimental measurement and the CFD modeling of Ref. [44]. Drophead velocity is directly linked to the bubble expansion rate. Most researchers normally adopt the Clausius-Clapeyron equation to predict bubble growth [16,48]. However, Ref. [44] utilized polytropic gas expansion to avoid using an additional thermal model to solve the temperature distribution. Regardless of this simplification, drophead velocity from their simulation matched well with experiment. Since the bubble explosive expansion happens in a few microseconds, the expansion rate and therefore drophead velocity may not be very different between these models. Another important parameter influencing drophead velocity is the nozzle geometry. Reference [16] showed that chamber and nozzle geometry will play an important role in projectile speed. The smaller the nozzle diameter, the higher the drophead velocity would be. The nozzle diameter in Ref. [44] is $20 \mu\text{m}$ while in our study it was $48 \mu\text{m}$. Their print head geometry cannot be utilized for

bioprinting because its nozzle diameter is small for injecting cells, $\sim 16 \mu\text{m}$. Moreover, the geometry of their print head is significantly more complicated compared to the HP60. Although different print head geometry is used in our simulation, it is observed that our numerical results roughly matches the experimental result and CFD simulation of Tan *et al.* [44]. The main reason for lower print head velocity is using a nozzle with a bigger diameter, $48 \mu\text{m}$, compared to Ref. [44] where it was $20 \mu\text{m}$.

Evidently, the temperature distribution is not uniform inside the saturated bubble. Thus, vapor density would be different in various locations of the affected region, and it is constantly changing in time. Moreover, due to continuous fluid motion, the pressure is also not uniform inside the chamber. The time history of minimum vapor density, maximum temperature, and maximum local pressure in the chamber are demonstrated in Figs. 16(a), 16(b), and 17, respectively. Due to high heat flux, the maximum local pressure, maximum temperature, and minimum vapor density in the most critical location of the nucleated bubble instantly reach the highest values of $\sim 20 \text{ Mpa}$, $\sim 600 \text{ }^\circ\text{C}$, and $\sim 140 \text{ kg/m}^3$, respectively. Thus,

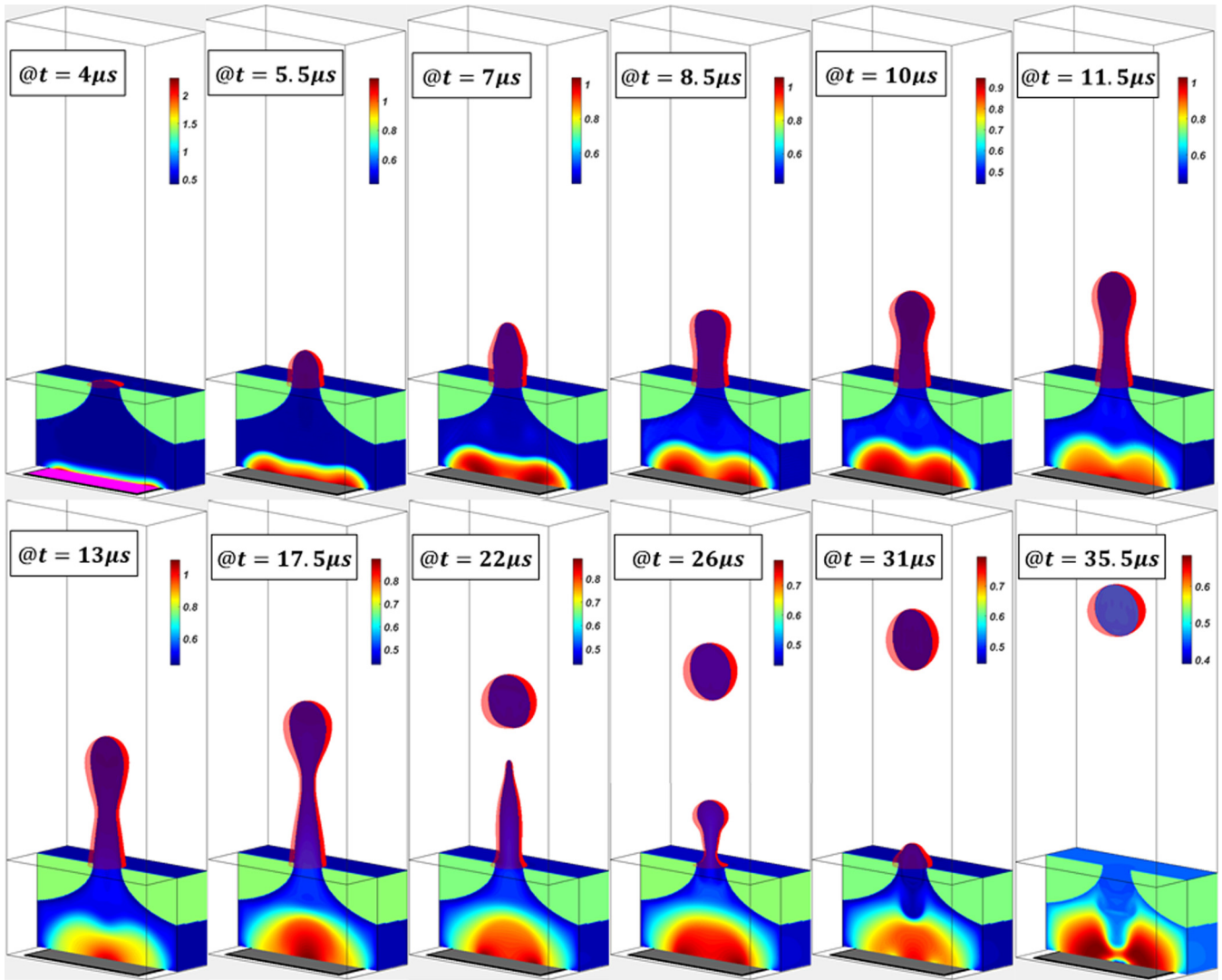


FIG. 13. Time sequence of droplet injection process at nozzle cross section. Color bar represents relative temperature.

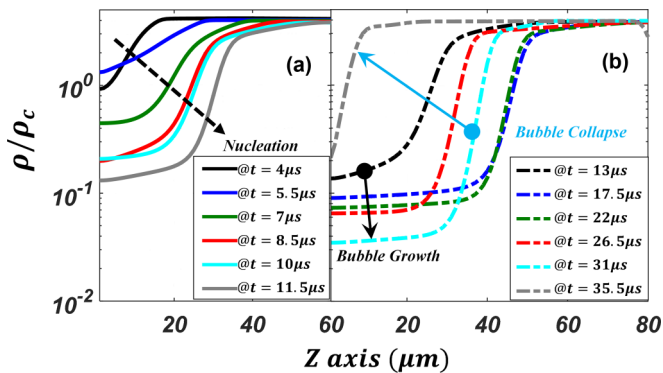


FIG. 14. Relative density distribution during nucleation, bubble growth, and bubble collapse (a) before and (b) after bubble coalescence. The density data shown are related to dashed lines shown in Fig. 12 at (a) $t = 4 \mu s$ and (b) $t = 13 \mu s$. (a) Black and gray solid lines represent density distribution at $t = 4 \mu s$ and $t = 11.5 \mu s$, respectively. (b) Black and gray dashed lines represent density distribution at $t = 13.5 \mu s$ and $t = 35.5 \mu s$, respectively.

the vapor thermodynamic state in the nucleated bubble is very close to the water critical point.

Furthermore, during bubble expansion, pressure, temperature, and density continuously decrease as shown in Figs. 16

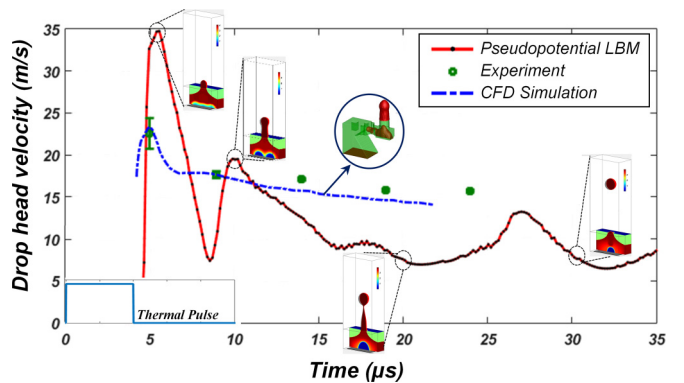


FIG. 15. Comparison of drop head velocity between experiment [44], CFD simulation of Tan *et al.* [44], and pseudopotential LB method in this study.

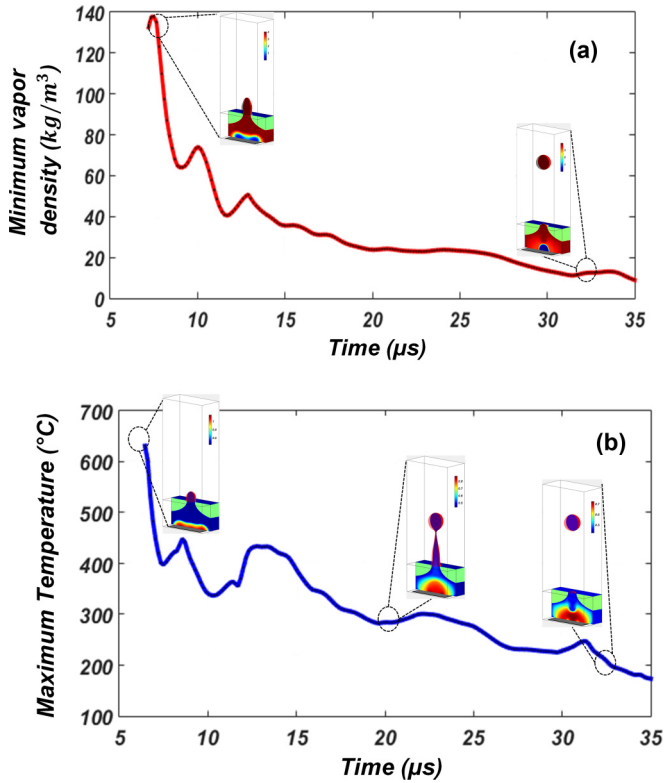


FIG. 16. The history of (a) minimum vapor density and (b) maximum local temperature from the pseudopotential LB method.

and 17. When the bubble reaches its maximum volume, the pressure energy has already converted to kinetic energy. As heat dissipates to the surrounding liquid, the saturated vapor pressure gradually decreases, resisting liquid water refilling the bubble. Finally, during the collapse stage, the maximum local pressure drastically decreases, and the bubble rapidly disappears in just $4\mu\text{s}$. Although previous CFD studies [13,44] did a nice job simulating the ejection dynamic, they lack a realistic bubble model. For instance, the maximum bubble pressure in Tan's model [13] is 2 Mpa, while we predict instantaneous saturated pressure as high as ~ 20 Mpa, which is closer to previously reported values of $\sim 12\text{--}15$ Mpa in

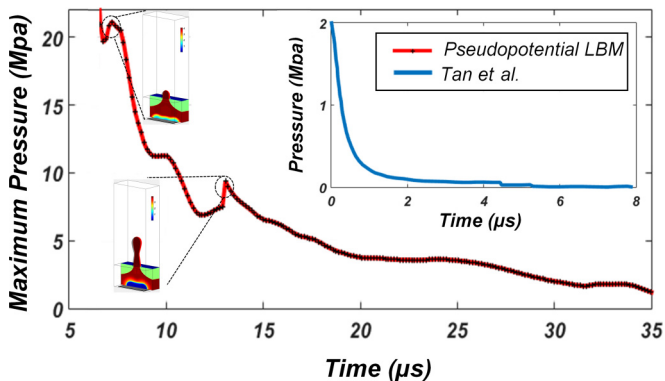


FIG. 17. Maximum local pressure derived from the pseudopotential LB method in this study compared to vapor pressure used in Ref. [13].

Ref. [16]. To discuss this in more detail, Asai *et al.* [49] reported that the saturated vapor pressure will reach 10–100 times as high as the atmospheric pressure. In their later study [50,51], initial bubble pressure was taken as 7.5 Mpa. It should be noted that bubble generation and collapse happen very fast, and vapor close to heating element is saturated during this period. Thus, the maximum bubble pressure should be at least 7.5 Mpa (saturated vapor pressure of water at $\sim 300^\circ\text{C}$) during nucleation. A recent study [17] used similar logic to assume an initial vapor pressure as an input to their model.

Compared to previous studies, inclusion of compressibility effect via direct implementation of EOS and phase transition using pseudopotential LBM and heat conduction through thermal LBM, all in one setup, makes our modeling more realistic. These features distinguish our modeling approach from previous conventional CFD methods where the vapor bubble was merely treated as a cavity [13,16,44–46]. Easy implementation of various models in one platform is one other advantage of the current method. Furthermore, easy parallelization of the LBM code can also significantly enhance computation speed.

V. CELL DAMAGE

Thermal injection has been successfully used for printing cells, yet it is difficult to evaluate potential cell damage in experiments [14,24,25,52,53]. To study membrane mechanical damage, we need to visualize deformation of the cell as it squeezes out of the nozzle head first. To model the bioprinting process, the cell membrane in its natural state is modeled as a floating sphere with a diameter of $16\mu\text{m}$. It consists of $N_v = 600$ vertex nodes connected by a linear spring with stiffness of $k_s = 5.6 \times 10^5 \mu\text{g s}^{-2}$. Moreover, the triangular network has bending stiffness, local area constraint stiffness, global area constraint stiffness, and volume constraint stiffness are $k_b = 9.0 \times 10^3 \mu\text{g } \mu\text{m}^2 \text{s}^{-2}$, $k_A = 2.7 \times 10^7 \mu\text{g s}^{-2}$, $k_a = 3.0 \times 10^6 \mu\text{g s}^{-2}$, and $k_v = 5.0 \times 10^6 \mu\text{g m}^{-1} \text{s}^{-2}$, respectively. During rapid explosive vapor expansion, the $16\mu\text{m}$ cell squeezes out of a $48\mu\text{m}$ nozzle and quickly reaches its most deformed state at $6.25\mu\text{s}$ as shown in Fig. 18. In the following, we briefly discuss cell deformation and damage during the thermal injection process.

Cui *et al.* experimentally investigated viability and pore development on a membrane of printed Chinese hamster ovary cells [24]. They used propidium iodide and dextran molecules of various molecular weights to stain the printed cells. Then they evaluated the cutoff molecular size of these agents penetrating the cell membrane. By doing so, they would be able to estimate pore size and better understand the transient nature of pores after printing. Measuring the fluorescence intensity of stained cells after 15 min, they confirmed the existence of 10.5 nm sized pores on the cell membrane. They also reported that the pore size gradually decreases over time and completely disappear after 2 h incubation.

Cell damage during printing process can be associated with thermal shock or mechanical deformation. According to our study, temperature rise to critical temperatures is mostly maintained within the vaporous region close to the heating element, and cells floating in the solution may rarely come in contact with this high-temperature zone. Additionally, pore

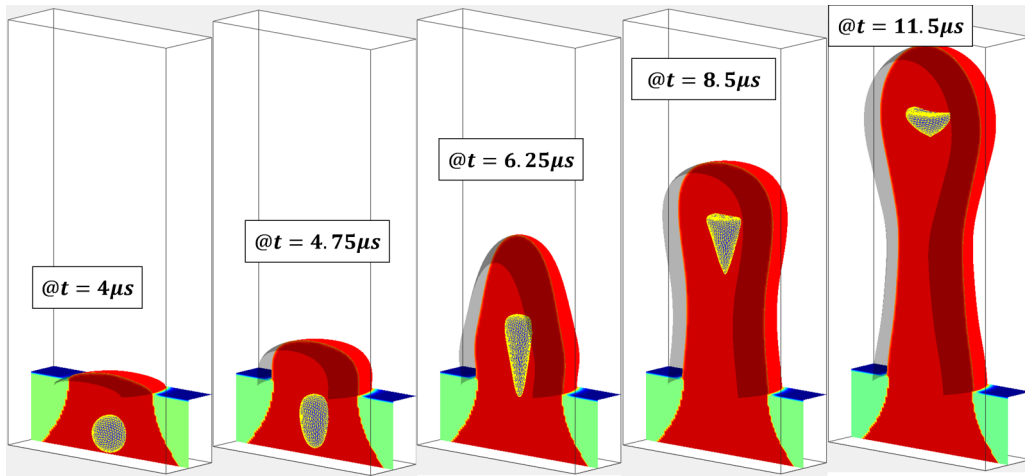


FIG. 18. Time sequence of cell deformation as it gets squeezed out of the nozzle printer.

formation on the cell membrane can be directly attributed to mechanical damage [24]. The transient nature of formed pores on the cell membrane suggest that mechanical deformation is the reason for the damage.

One important factor which strongly influences the mechanical resistance of cell membrane is loading speed. Koshiyama and Wada [54] carried out numerical simulations studying pore formation dynamics under various loading conditions. They specifically focused on the effect of stretching speeds on the pore formation process. They performed equibiaxial stretching simulations on a bilayer patch with pulling speeds of 0.1, 0.3, and 1.0 m s⁻¹. Their molecular dynamic simulation results indicated that multipores are more likely to form under higher stretching speeds. Pore formation under mechanical loading at the molecular level is a statistical phenomenon. Thus, Koshiyama and Wada [54] present their results for the average chance of pore formation as a function of areal strain using an error function. For instance, at a certain stretching speed and areal strain, we can look up the probability of pore formation as shown in Fig. 19(e). For more detailed information on this topic, readers can refer to our previous work [33] where we studied the mechanical damage of an RBC membrane under high shear flows.

Under a quasistatic loading condition, we will have 100% pore formation at areal strain 1.2, and progressive pore growth on the cell membrane will eventually lead to cell rupture; see Fig. 19(e). However, at a higher loading speed, the pores start to form at a much higher areal strain. Thus, to further study mechanical deformation leading to pore formation, we analyze membrane deformation at its most stretched state. Areal strain, stretching speed, maximum axial stress, and maximum shear stress distribution on the cell membrane are plotted at 6.25 μs in Figs. 19(a)–19(d). It is observed that areal strain can reach 0.85 during a very short time under a high loading speed of ~ 0.2 m s⁻¹. An equibiaxial stretching assumption is used for the calculation of this loading speed [54]. However, the stretching speed in a critical direction can even reach 1.5 m s⁻¹. In this condition, the maximum areal strain of the membrane falls well below the critical threshold, proving that cells are most likely to survive printing process. Even for cases with smaller nozzles, cell viability will not drop significantly as long as the maximum areal strain is maintained below the acceptable range. Moreover, according to Ref. [54] at these high deformation and loading speeds, the squeezing energy will be released through creation of multiple smaller pores rather than one bigger pore [54]. Thus, the increase in loading

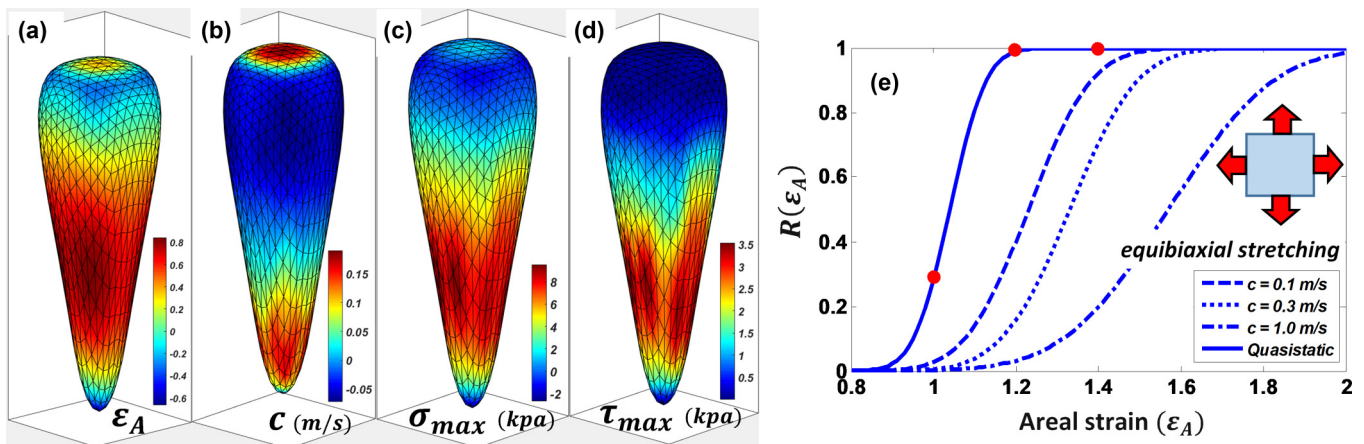


FIG. 19. (a) Areal strain, (b) stretching speed, (c) maximum axial stress, and (d) maximum shear stress distribution on cell membrane at 6.25 μs. (e) The probability of pore formation $R(\epsilon_A)$ at various stretching speeds [54].

rate will result in increase in rupture tension [55]. In other words, a high loading rate retards formation of big pores and accordingly the cell rupture [56].

VI. CONCLUSIONS

Pseudopotential LBM is very capable of modeling phase transitions. However, it is unstable at ambient temperature. Due to this limitation, the pseudopotential thermal LBM has not yet been applied to complex phase-changing applications at ambient temperature. We proposed a approach which utilize temperature-dependent reduced parameters to overcome this limitation. It allows us to look into instantaneous phase-changing phenomena with a local high-temperature gradient which has not been done before to the best of our knowledge. Using this method, we are also able to concurrently simulate heat transfer, phase transition, and fluid-cell interaction in one platform. While previous thermal ejection simulations treated bubble vapor artificially as a cavity, vapor and liquid densities in our approach are directly linked to temperature and pressure in a physical way through a nonideal EOS, and the only input to the computational domain is the heat pulse at the lower boundary. Furthermore, all temperature-dependent fluid properties are also constantly being updated during the simulation. Overall, we showed that we simulate bubble nucleation and growth more realistically. Furthermore, our simulation is capable of studying whether and how mechanical or heat shock will damage cells in bioprinting. To model the bioprinting

process, we coupled our modified pseudopotential thermal LBM formulation with a spring network model through the immersed boundary method. Cell deformation is visualized as it squeezes out of the nozzle head. It was observed that that fast deformation of a cell membrane can significantly increase rupture tension. Following goals have been achieved in this paper:

(1) Introduce and utilize a temperature-dependent reduced parameter to stabilize the pseudopotential method at room temperature.

(2) Simulate various phenomena such as phase transition, heat transfer, cell deformation, and wall-liquid interaction in one platform.

(3) Present a more realistic simulation of bubble nucleation, growth, and collapse by directly implementing nonideal EOS of water into an LBM formulation.

(4) Provide better insights into mechanical damage of cell membrane during a drop-on demand cell printing process.

For future work, the pseudopotential model can be used in conjunction with an adaptive mesh method to minimize the interface thickness. We also encounter some instability difficulties which can be probably avoided by using a multirelaxation method in the future.

ACKNOWLEDGMENT

This work is supported by the National Institutes of Health (NIH) (Grant R01HL131750).

-
- [1] S. Sohrabi, M. S. Saidi, M. Saadatmand, M. H. Banazadeh, and B. Firoozabadi, Three-dimensional simulation of urine concentrating mechanism in a functional unit of rat outer medulla. I. Model structure and base case results, *Math. Biosci.* **258**, 44 (2014).
- [2] S. Sohrabi, S. Wang, J. Tan, J. Xu, J. Yang, and Y. Liu, Nanoparticle transport and delivery in a heterogeneous pulmonary vasculature, *J. Biomech.* **50**, 240 (2017).
- [3] S. Wang, S. Sohrabi, J. Xu, J. Yang, and Y. Liu, Geometry design of herringbone structures for cancer cell capture in a microfluidic device, *Microfluid. Nanofluid.* **20**, 148 (2016).
- [4] Rajabzadeh-H. Oghaz, N. Varble, J. M. Davies, A. Mowla, H. J. Shakir, A. Sonig *et al.*, Computer-assisted adjuncts for aneurysmal morphologic assessment: Toward more precise and accurate approaches, in *Medical Imaging 2017: Computer-Aided Diagnosis* (International Society for Optics and Photonics, 2017), p. 101341C.
- [5] P. Yuan and L. Schaefer, Equations of state in a lattice Boltzmann model, *Phys. Fluids* **18**, 042101 (2006).
- [6] A. Fakhari, D. Bolster, and L.-S. Luo, A weighted multiple-relaxation-time lattice Boltzmann method for multiphase flows and its application to partial coalescence cascades, *J. Comput. Phys.* **341**, 22 (2017).
- [7] A. Hu, L. Li, S. Chen, Q. Liao, and J. Zeng, On equations of state in pseudo-potential multiphase lattice Boltzmann model with large density ratio, *Int. J. Heat Mass Transf.* **67**, 159 (2013).
- [8] S. Gong and P. Cheng, Numerical investigation of droplet motion and coalescence by an improved lattice Boltzmann model for phase transitions and multiphase flows, *Comput. Fluids* **53**, 93 (2012).
- [9] X. Shan and H. Chen, Lattice Boltzmann model for simulating flows with multiple phases and components, *Phys. Rev. E* **47**, 1815 (1993).
- [10] M. R. Swift, W. Osborn, and J. Yeomans, Lattice Boltzmann Simulation of Nonideal Fluids, *Phys. Rev. Lett.* **75**, 830 (1995).
- [11] A. Fakhari, M. Geier, and D. Bolster, A simple phase-field model for interface tracking in three dimensions, *Comput. Math. Appl.* (2016), doi:10.1016/j.camwa.2016.08.021.
- [12] A. Kupershtokh, D. Medvedev, and D. Karpov, On equations of state in a lattice Boltzmann method, *Comput. Math. Appl.* **58**, 965 (2009).
- [13] H. Tan, An adaptive mesh refinement based flow simulation for free-surfaces in thermal inkjet technology, *Int. J. Multiphase Flow* **82**, 1 (2016).
- [14] W. C. Wilson and T. Boland, Cell and organ printing 1: Protein and cell printers, *Anat. Rec.* **272A**, 491 (2003).
- [15] S.-W. Lee, H.-C. Kim, K. Kuk, and Y.-S. Oh, A monolithic inkjet print head: DomeJet, *Sens. Actuators A* **95**, 114 (2002).

- [16] H. Zhou and A. Gué, Simulation model and droplet ejection performance of a thermal-bubble microjector, *Sens. Actuators B* **145**, 311 (2010).
- [17] Y. Suh and G. Son, A level-set method for simulation of a thermal inkjet process, *Numer. Heat Transfer B* **54**, 138 (2008).
- [18] O. Ruiz, CFD model of the thermal inkjet droplet ejection process. *ASME/JSME 2007 Thermal Engineering Heat Transfer Summer Conference, Vancouver, British Columbia, Canada, July 8–12, 2007* (ASME, 2007), Vol. 3, pp. 357–365.
- [19] T. Lindemann, D. Sassano, A. Bellone, R. Zengerle, P. Koltay, and I. Olvetti, Three-dimensional CFD-simulation of a thermal bubble jet printhead, in *NSTI Nanotechnology Conference and Trade Show, Boston Sheraton Hotel & Copley Convention Center, Massachusetts, March 7-11, 2004* (NSTI, 2004), pp. 227–230.
- [20] N. Nikolopoulos, K.-S. Nikas, and G. Bergeles, A numerical investigation of central binary collision of droplets, *Comput. Fluids* **38**, 1191 (2009).
- [21] W. Lee and G. Son, Numerical study of droplet impact and coalescence in a microline patterning process, *Comput. Fluids* **42**, 26 (2011).
- [22] H. Rajabzadeh-Oghaz, B. Firoozabadi, M. S. Saidi, M. Monjezi, M. A. N. Shirazi, and E. M. Rad, Pulsatile blood flow in total cavopulmonary connection: A comparison between Y-shaped and T-shaped geometry, *Med. Biol. Eng. Comput.* **55**, 213 (2017).
- [23] A. Foroughi, S. Green, and B. Stoeber, Optical transparency of paper as a function of moisture content with applications to moisture measurement, *Rev. Sci. Instrum.* **87**, 023706 (2016).
- [24] X. Cui, D. Dean, Z. M. Ruggeri, and T. Boland, Cell damage evaluation of thermal inkjet printed Chinese hamster ovary cells, *Biotechnol. Bioeng.* **106**, 963 (2010).
- [25] E. A. Roth, T. Xu, M. Das, C. Gregory, J. J. Hickman, and T. Boland, Inkjet printing for high-throughput cell patterning, *Biomaterials* **25**, 3707 (2004).
- [26] X. Cui, T. Boland, D. D. D’Lima, and M. K. Lotz, Thermal inkjet printing in tissue engineering and regenerative medicine, *Recent Pat. Drug Deliv. Form.* **6**, 149 (2012).
- [27] W. K. Liu, Y. L. Liu, D. Farrell, L. Zhang, X. S. Wang, Y. Fukui *et al.*, Immersed finite element method and its applications to biological systems, *Comput. Methods Appl. Mech.* **195**, 1722 (2006).
- [28] J. Tan, S. Wang, J. Yang, and Y. Liu, Coupled particulate and continuum model for nanoparticle targeted delivery, *Comput. Struct.* **122**, 128 (2013).
- [29] S. Sohrabi, J. Zheng, E. A. Finol, and Y. Liu, Numerical simulation of particle transport and deposition in the pulmonary vasculature, *J. Biomech. Eng.* **136**, 121010 (2014).
- [30] S. Gong and P. Cheng, Lattice Boltzmann simulation of periodic bubble nucleation, growth and departure from a heated surface in pool boiling, *Int. J. Heat Mass Transf.* **64**, 122 (2013).
- [31] Z. Guo, B. Shi, and C. Zheng, A coupled lattice BGK model for the Boussinesq equations, *Int. J. Numer. Methods Fluids* **39**, 325 (2002).
- [32] S. Gong and P. Cheng, A lattice Boltzmann method for simulation of liquid–vapor phase-change heat transfer, *Int. J. Heat Mass Transf.* **55**, 4923 (2012).
- [33] S. Sohrabi and Y. Liu, A cellular model of shear-induced hemolysis, *Artificial Organs* **41**, E80 (2017).
- [34] D. Fedosov, B. Caswell, and G. E. Karniadakis, Coarse-grained red blood cell model with accurate mechanical properties, rheology and dynamics, in *Engineering in Medicine and Biology Society, Annual International Conference of the IEEE (IEEE, 2009)*, pp. 4266–4269.
- [35] D. A. Fedosov, J. Fornleitner, and G. Gompper, Margination of White Blood Cells in Microcapillary Flow, *Phys. Rev. Lett.* **108**, 028104 (2012).
- [36] Y. Ujihara, M. Nakamura, H. Miyazaki, and S. Wada, Proposed spring network cell model based on a minimum energy concept, *Ann. Biomed. Eng.* **38**, 1530 (2010).
- [37] D. A. Fedosov, B. Caswell, and G. E. Karniadakis, A multiscale red blood cell model with accurate mechanics, rheology, and dynamics, *Biophys. J.* **98**, 2215 (2010).
- [38] Y. Ujihara, M. Nakamura, and H. Miyazaki, Effects of the initial orientation of actin fibers on global tensile properties of cells, *J. Biomech. Sci. Eng.* **5**, 515 (2010).
- [39] C. S. Peskin, The immersed boundary method, *Acta Numerica* **11**, 479 (2002).
- [40] C. S. Peskin and D. M. McQueen, A three-dimensional computational method for blood flow in the heart I. Immersed elastic fibers in a viscous incompressible fluid, *J. Comput. Phys.* **81**, 372 (1989).
- [41] J. Tan, W. Keller, S. Sohrabi, J. Yang, and Y. Liu, Characterization of nanoparticle dispersion in red blood cell suspension by the lattice Boltzmann-immersed boundary method, *Nanomaterials* **6**, 30 (2016).
- [42] M. Abkarian, M. Faivre, and A. Viallat, Swinging of Red Blood Cells Under Shear Flow, *Phys. Rev. Lett.* **98**, 188302 (2007).
- [43] Q. Zou and X. He, On pressure and velocity boundary conditions for the lattice Boltzmann BGK model, *Phys. Fluids* **9**, 1591 (1997).
- [44] H. Tan, E. Tornaiainen, D. P. Markel, and R. N. Browning, Numerical simulation of droplet ejection of thermal inkjet printheads, *Int. J. Numer. Methods Fluids* **77**, 544 (2015).
- [45] A. Sen and J. Darabi, Droplet ejection performance of a monolithic thermal inkjet print head, *J. Micromech. Microeng.* **17**, 1420 (2007).
- [46] A.-S. Yang and W.-M. Tsai, Ejection process simulation for a piezoelectric microdroplet generator, *J. Fluids Eng.* **128**, 1144 (2006).
- [47] See Supplemental Material at <http://link.aps.org/supplemental/10.1103/PhysRevE.97.033105> for a short video demonstrating density distribution during droplet ejection process.
- [48] Y. Hong, N. Ashgriz, J. Andrews, and H. Parizi, Numerical simulation of growth and collapse of a bubble induced by a pulsed microheater, *J. Microelectromech. Syst.* **13**, 857 (2004).
- [49] A. Asai, T. Hara, and I. Endo, One-dimensional model of bubble growth and liquid flow in bubble jet printers, *Japanese Journal of Applied Physics* **26**, 1794 (1987).
- [50] A. Asai, Three-dimensional calculation of bubble growth and drop ejection in a bubble jet printer, *J. Fluids Eng.* **114**, 638 (1992).
- [51] A. Asai, Application of the nucleation theory to the design of bubble jet printers, *Jpn. J. Appl. Phys.* **28**, 909 (1989).

- [52] X. Cui and T. Boland, Human microvasculature fabrication using thermal inkjet printing technology, *Biomaterials* **30**, 6221 (2009).
- [53] T. Xu, C. A. Gregory, P. Molnar, X. Cui, S. Jalota, S. B. Bhaduri *et al.*, Viability and electrophysiology of neural cell structures generated by the inkjet printing method, *Biomaterials* **27**, 3580 (2006).
- [54] K. Koshiyama and S. Wada, Molecular dynamics simulations of pore formation dynamics during the rupture process of a phospholipid bilayer caused by high-speed equibiaxial stretching, *J. Biomech.* **44**, 2053 (2011).
- [55] T. Shigematsu, K. Koshiyama, and S. Wada, Effects of stretching speed on mechanical rupture of phospholipid/cholesterol bilayers: Molecular dynamics simulation, *Sci. Rep.* **5**, 15369 (2015).
- [56] E. Evans, V. Heinrich, F. Ludwig, and W. Rawicz, Dynamic tension spectroscopy and strength of biomembranes, *Biophys. J.* **85**, 2342 (2003).